



Published in final edited form as:

Cell Syst. 2022 April 20; 13(4): 334–345.e5. doi:10.1016/j.cels.2022.01.002.

Directed mutational scanning reveals a balance between acidic and hydrophobic residues in strong human activation domains

Max V. Staller^{1,2,3,*}, Eddie Ramirez^{1,2}, Sanjana R. Kotha³, Alex S. Holehouse^{4,5}, Rohit V. Pappu^{5,6}, Barak A. Cohen^{1,2,7,*}

¹Edison Family Center for Genome Sciences and Systems Biology, Washington University School of Medicine in St. Louis, Saint Louis, MO 63110, USA

²Department of Genetics, Washington University School of Medicine in St. Louis, Saint Louis, MO 63110, USA

³Center for Computational Biology, University of California Berkeley, Berkeley, CA 94720, USA

⁴Department of Biochemistry and Molecular Biophysics, Washington University School of Medicine in St. Louis, Saint Louis, MO 63110, USA

⁵Center for Science and Engineering of Living Systems, Washington University in St. Louis, St. Louis, MO 63130, USA

⁶Department of Biomedical Engineering, Washington University in St. Louis, St. Louis, MO 63130, USA

⁷Lead contact

SUMMARY

Acidic activation domains are intrinsically disordered regions of the transcription factors that bind coactivators. The intrinsic disorder and low evolutionary conservation of activation domains have made it difficult to identify the sequence features that control activity. To address this problem, we designed thousands of variants in seven acidic activation domains and measured their activities with a high-throughput assay in human cell culture. We found that strong activation domain activity requires a balance between the number of acidic residues and aromatic and leucine residues. These findings motivated a predictor of acidic activation domains that scans the human proteome for clusters of aromatic and leucine residues embedded in regions of high acidity. This predictor identifies known activation domains and accurately predicts previously unidentified ones.

This is an open access article under the CC BY-NC-ND license (<http://creativecommons.org/licenses/by-nc-nd/4.0/>).

*Correspondence: mstaller@berkeley.edu (M.V.S.), cohen@wustl.edu (B.A.C.).

AUTHOR CONTRIBUTIONS

M.V.S. and B.A.C. designed the project and wrote the manuscript. M.V.S. and E.R. collected the data. M.V.S., E.R., S.R.K., and A.S.H. analyzed the data. R.V.P. and B.A.C. interpreted the data. All authors edited the manuscript.

DECLARATION OF INTERESTS

The authors declare no competing interests.

SUPPLEMENTAL INFORMATION

Supplemental information can be found online at <https://doi.org/10.1016/j.cels.2022.01.002>.

INCLUSION AND DIVERSITY

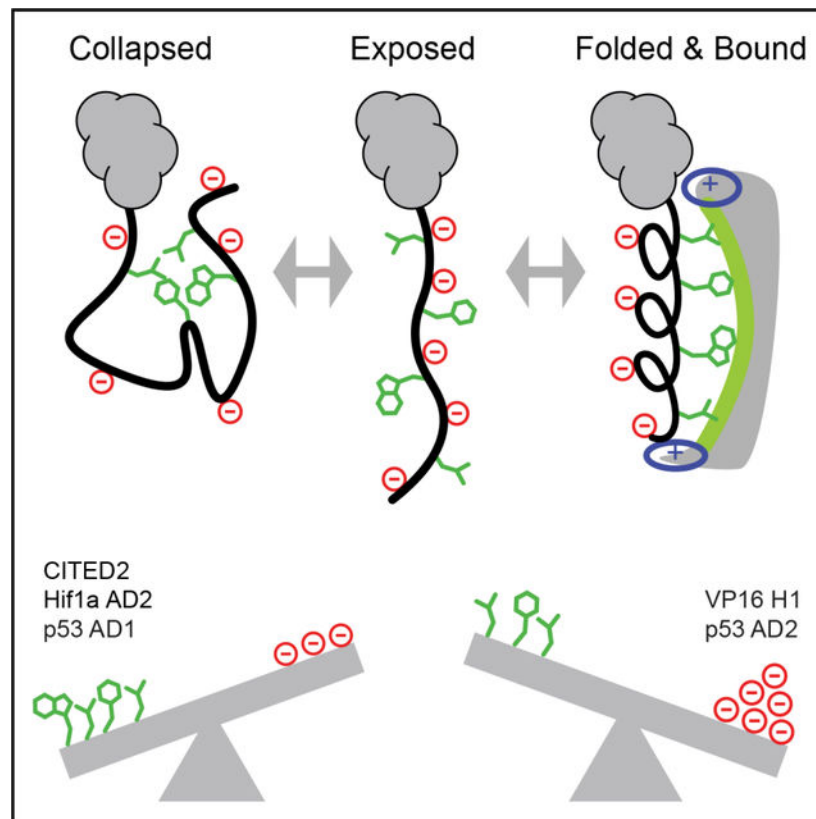
One or more of the authors of this study self-identifies as an underrepresented ethnic minority in science. One or more of the authors of this study received support from a program designed to increase minority representation in science.

Our results support a flexible acidic exposure model of activation domains in which the acidic residues solubilize hydrophobic motifs so that they can interact with coactivators. A record of this paper's transparent peer review process is included in the supplemental information.

In brief

Transcriptional activation domains are poorly conserved, intrinsically disordered regions of the transcription factors that remain difficult to predict from protein sequences. A high-throughput method reveals how strong activation domains require a balance between acidic and hydrophobic residues. This balance powers an accurate predictor of activation domains on human transcription factors.

Graphical Abstract



INTRODUCTION

Transcription factors (TFs) activate gene expression using DNA binding domains (DBDs) and activation domains (ADs). DBDs are structured, evolutionarily conserved, and bind related DNA sequences (Latchman, 2008). ADs are intrinsically disordered, poorly conserved, and bind structurally diverse coactivator subunits (Dyson and Wright, 2016). Bioinformatics tools can predict the DBDs from protein sequence, but there are few tools for predicting ADs (El-Gebali et al., 2019; Finn et al., 2016). When a new genome is

sequenced, scanning for DBDs can predict candidate TFs, but it is not possible to predict which candidate TFs contain ADs.

Predicting ADs from amino acid sequences has been difficult for five reasons: (1) ADs have diverse primary sequences (Latchman, 2008), (2) ADs have poor sequence conservation that hinders comparative genomics, (3) ADs are intrinsically disordered and have diverse modes of binding coactivators (Dyson and Wright, 2016), (4) until recently, measuring AD activity has been low throughput, and (5) the key sequence properties that control AD activity remain unresolved. Many ADs are acidic (have a net negative charge), but site-directed mutagenesis has shown that clusters of hydrophobic residues, called motifs, make the largest contributions to activity (Cress and Triezenberg, 1991; Dyson and Wright, 2016; Warfield et al., 2014). Here, we test the hypothesis that ADs are composed of hydrophobic motifs surrounded by an acidic context.

Based on our work on yeast (Staller et al., 2018), we developed an *acidic exposure model* for AD function: acidity and intrinsic disorder keep hydrophobic motifs exposed to solvent where they are available to bind coactivators (Figure 1A). Hydrophobic residues tend to interact with each other and drive intramolecular chain collapse, suppressing interactions with coactivators. Surrounding the hydrophobic residues with acidic residues that repel one another exposes the motifs to solvent, promoting interactions with coactivators. For example, in the VP16 AD, the critical F442 is highly exposed to solvent in solution, but exposure decreases upon coactivator binding (Shen et al., 1996a, 1996b). Three recent studies on yeast (Erijman et al., 2020; Ravarani et al., 2018; Sanborn et al., 2021) also found that strong ADs contain both acidic and hydrophobic residues, which supports the acidic exposure model. However, whether this model can explain the properties of human ADs remains unknown.

Here, we show that the acidic exposure model extends from yeast to human cells. We introduce a high-throughput reporter system to test more than 3,500 variants in seven ADs. We designed these variants to interrogate two aspects of the acidic exposure model—acidic residues and aromatic residues. We found that strong ADs balance the number of acidic residues against the number of aromatic and leucine residues. Based on these results, we found that scanning the proteome for clusters of eight amino acids (acidic, basic, aromatic, and leucine residues) was sufficient to accurately predict new and known ADs. Taken together, our results suggest that the acidic exposure model may be a general explanation for the function of the eukaryotic ADs, from those in yeast to those in humans, and provide a framework for unifying the roles of acidity, hydrophobicity, and intrinsic disorder in acidic ADs.

RESULTS

To test the acidic exposure model, we developed a high-throughput method to assay the AD variants in parallel in human cell culture (Figure 1B). We engineered a cell culture system with a synthetic TF that binds and activates a genome-integrated GFP reporter. Each cell receives one AD variant marked by a unique DNA barcode integrated into the same genomic “landing pad” with Cre recombinase and asymmetric loxP sites. The landing

pad equalizes the effects of genomic position on expression (Maricque et al., 2018). The synthetic TF contains an mScarlet red fluorescent protein for measuring abundance, but after trying four different red fluorescent proteins, each with low signal, we did not normalize for protein abundance in this study. To avoid cell toxicity, the synthetic TF contains an engineered DBD (Park et al., 2019) and an estrogen response domain for inducible nuclear localization (McIsaac et al., 2013). AD variants that drive different levels of GFP expression are separated by fluorescent activated cell sorting (FACS), and the barcodes in each sorted pool are counted by deep sequencing (Kinney et al., 2010; Sharon et al., 2012; Staller et al., 2018). We used the barcode counts to compute a probability mass function for each AD across the four pools and the GFP signal of each pool to compute a weighted average GFP signal. The assay is reproducible (average Pearson correlation between replicates of 0.69) and recapitulates the activity of known mutations in human ADs (Figure S1). A synthetic TF without an AD (No AD control) was used to define baseline activity in our assay. In the library, the ADs are cloned into the N terminus of the synthetic TF, between the ATG start codon (M) and a GSGS linker. In the No AD control plasmid, nothing is between the initial M and the GSGS linker. We combined biological replicates by normalizing the activity of the No AD control to 2,000 (arbitrary fluorescence units, AU, STAR Methods) and averaging the fluorescence values together.

In our first experiment, we performed deep mutational scans (DMS, where every position is mutated to all 19 other residues) and rational mutagenesis on the two ADs of the tumor suppressor TF, p53. This library contained 2,991 variants, each paired with 5 barcodes. After an extensive analysis, we determined that most point substitutions had small effects on activity and that five barcodes were not sufficient to resolve these small changes in activity. DMS have been very informative for structured proteins (Gray et al., 2017) but not for intrinsically disordered regions, where most point substitutions do not cause measurable changes in activity (Giacomelli et al., 2018; Majithia et al., 2016). In the rational mutagenesis, we introduced multiple substitutions to test the roles of acidic residues, aromatic residues, and intrinsic disorder. These perturbations had large effects on activity that could be resolved with five barcodes (Figures S1 and S2).

In our second experiment, we examined 525 rationally designed variants of five ADs, each tagged with twenty-eight barcodes. Using more barcodes allowed us to resolve smaller changes in activity, and assaying mutations with larger effect sizes increased the measurement reproducibility (Figure S1). We focused the main text on these high-quality data and used the noisier p53 data to corroborate trends.

Using this assay, we investigated three key features of acidic ADs—acidic residues, hydrophobic motifs, and disorder-to-order transitions (Figure 1C). We designed sequence variants that systematically added and subtracted acidic residues or aromatic residues in seven ADs—VP16 (H1 region, 415–453), Hif1 α (AD2, 781–896), CITED2 (220–258), Stat3 (719–764), p65 (AD2, 521–551), p53 AD1 (1–40), and p53 AD2 (40–60) (Berlow et al., 2017; Brady et al., 2011; Lecoq et al., 2017; Raj and Attardi, 2017; Regier et al., 1993; Vogel et al., 2015; Wojciak et al., 2009). Most variants had five or fewer substitutions (Figure 1D). For each AD, we hand-designed 6–10 “supercharge” variants that added aromatic residues next to the existing acidic residues and acidic residues next to the existing

aromatic residues. For each disordered region that folds into an alpha helix upon coactivator binding, we introduced proline or glycine residues to break the helices (Figure S3). The complete list of substitutions and activities are located in Data S1 (VP16, Hif1 α , CITED2, Stat3, p65. 525 variants, 28 barcodes per variant, and 4 replicates) and Data S2 (p53 AD1, p53 AD2. 2,991 variants, 5 barcodes per variant, and 3 replicates). Note that the activity values in the two experiments are not comparable because they were collected on different cell sorters and normalized differently.

Compared with the No AD control, all ADs activated the GFP reporter (Figures 2 and S2). For each AD, we identified variants that significantly changed activity after correction for multiple hypotheses (two-sided t test and 5% FDR, Dataset 1). For VP16, CITED2, and Hif1 α , we recovered variants that increased or decreased their activities (Dataset 1; Figure 2A). p65 and Stat3 were weakly active in the assay, reducing our sensitivity, and none of these variants significantly changed activity after correction for multiple hypotheses (Dataset 1). Either our assay was not sensitive enough to interrogate these two ADs or the residues we mutated made small contributions to activity.

Hydrophobic motifs are necessary for AD activity

We confirmed that hydrophobic motifs make large contributions to AD activity. We included published motifs (LPEL in CITED2, LPQL and LLxxL in Hif1 α , and LxxFxL in VP16 [Berlow et al., 2017; Freedman et al., 2003; Regier et al., 1993]) and predicted additional motifs by looking for clusters of W,F,Y,L,M residues. Substituting all the residues that comprise a motif with alanine residues decreased activity (Figures 2B and S2). In CITED2 and VP16, every cluster of the tested aromatic and leucine residues contributed to activity.

Acidic residues are necessary for AD activity

We systematically increased and decreased the net negative charge of each AD and plotted the resulting activities (Figures 3A and S2). For CITED2, Hif1 α , VP15, p53 AD1, and p53 AD2, acidic residues were necessary for full activity, and the regression of activity against net charge had significant negative slopes (Figures 3A, S2C, and S4A). For CITED2, Hif1 α , and VP16, slopes were significant when using the charge variants or all variants. Removing negatively charged residues (D and E) had effects similar to that of adding positively charged (K and R) residues and vice versa (Figure S5), suggesting that net charge and not residue identity is the key parameter.

For ADs with moderate acidity (CITED2, Hif1 α , and p53 AD1), adding acidic residues increased activity in most variants (Figure 3A). For p53 AD1, this effect mirrors how phosphorylation increases activity (Raj and Attardi, 2017). For the more acidic p53 AD2, adding acidic residues rarely increased activity; for the most acidic AD, VP16, adding acidic residues never increased activity. Thus, the starting net charge of the wild-type AD determined whether it was possible to increase activity by adding acidic residues.

For CITED2 and Hif1 α , adding acidic residues could either increase or decrease activity (Figure 3A: red versus blue) depending on the location of the substitution (Figure 3B). For CITED2, the variants with increased activity (Figure 3A, red) frequently added acidic residues in the flanks, near the hydrophobic motifs (Figures 3B and 3C, red), whereas the

variants with decreased activity frequently removed the positive residues in the center of the AD (Figures 3B and 3C, blue). For Hif1 α , the variants with increased activity were more likely to add acidic residues in the C terminus near L812, L813, or L819 or to remove R820. These data suggest that the location of the added acidic residues can determine how they modulate activity. This result agrees with our work in yeast and two random peptide screens that found that [DE][WFY] dipeptides make large contributions to AD activity (Erijman et al., 2020; Ravarani et al., 2018; Staller et al., 2018). To further test this idea, we used the Omega statistic to quantify how the mixture of aromatic and leucine (W,F,Y,L) residues with acidic residues (D,E) is related to activity (Martin et al., 2016). We found a modest correlation: variants with more evenly mixed W,F,Y, L and D,E (i.e., low Omega values) had higher activities (Figure S4D). Together with the literature, our data support the idea that the acidic residues near key hydrophobic motifs boost activity. For VP16, we could not increase activity by adding acidic residues, perhaps because 5/7 residues in the motifs are already adjacent to acidic residues. VP16 is the most acidic AD we examined and appears to be saturated for the effect of negative charge on activity.

Context-dependent effects of adding acidic or aromatic residues

When we systematically added and removed aromatic residues, we saw expected and unexpected changes in AD activity. Based on experiments in human cell culture with the VP16, p53, and ETS Variant transcription factor (ETV) family of ADs, we expected aromatic residues to be critical for activity and that adding aromatic residues would increase activity (Currie et al., 2017; Raj and Attardi, 2017; Regier et al., 1993). The VP16 variants generally matched this expectation: any substitution in F442 (A,L,W,Y) decreased activity. Furthermore, adding up to four aromatic residues increased activity in most cases (Figures 2B, 4A, and S6C). Similarly, for both p53 ADs, removing aromatics decreased activity and adding aromatic residues increased activity (Figure S2D).

However, in CITED2, adding and removing aromatic residues did not yield the expected results. Mutating the aromatic residues to alanine led to small decreases in activity, and mutating the aromatic residues to leucine residues caused small increases in activity (Figures 4A and S6A). Adding aromatic residues decreased activity for all but one variant. If, instead, we plot activity against the number of W,F,Y,L residues, CITED2 activity peaks at the WT number, 10 (Figures 4B and S4C).

In Hif1 α , adding or removing aromatic residues generally did not change activity. Mutating the lone Y to L caused a small, and not significant, increase in activity. Adding aromatic residues to Hif1 α caused small, and frequently not significant, decreases in activity (Figures S4B and S6B).

We saw two responses to adding acidic residues and two responses to adding aromatic residues. For the moderately acidic ADs, CITED2 and Hif1 α , we could increase activity by adding acidic residues and for CITED2, decrease activity by adding aromatic residues. For the more acidic ADs, VP16 and p53 AD2, we could increase activity by adding aromatic residues but not by adding acidic residues. Even for VP16, adding more than 4 aromatic residues always decreased activity, suggesting that for all ADs, there is a regime where adding aromatic residues will eventually decrease activity.

The acidic exposure model can explain why the responses to adding acidic residues mirror the opposite responses to adding aromatic residues. The model predicts that adding acidic residues will increase AD activity only when there are hydrophobic motifs that can be further exposed. Once the hydrophobic motifs are maximally exposed, adding more acidic residues will not increase activity. By contrast, adding more aromatic residues can increase activity only when there is excess acidity to keep these added residues exposed. Adding too many aromatic residues eventually reduces activity because they overwhelm the acidic residues and drive chain collapse. Thus, a prediction of the acidic exposure model is that acidic residues promote expanded AD conformations, whereas aromatic residues promote chain collapse. We tested this prediction with all-atom Monte Carlo simulations of the VP16 and CITED2 variants (STAR Methods) (Staller et al., 2018; Vitalis and Pappu, 2009) and calculated the radius of gyration, which captures the size of the conformational ensemble. Although the dispersion in the predicted radius of gyration is large for any given net charge, we found that adding acidic residues increases the radius of gyration, consistent with expansion (Figure S7A), and adding aromatic residues decreased the radius of gyration, consistent with partial chain collapse (Figure S7B). These trends hold true for the supercharge variants that add both aromatic and acidic residues (Figure S7C).

Leucine residues are critical for AD activity

We found that leucine residues made large contributions to activity. In yeast ADs, aromatic residues contribute more to activity than smaller hydrophobic residues such as leucine and methionine (Erijman et al., 2020; Jackson et al., 1996; Ravarani et al., 2018; Staller et al., 2018). In human cells, VP16 and both p53 ADs fit the following pattern: substituting aromatic residues decreased activity (Figures 2B, 4A, S2, and S4) (Cress and Triezenberg, 1991; Lin et al., 1994). However, in VP16, “motif 2” contains only leucine residues and is necessary for full AD activity (Figure 2C). In CITED2, summarizing the activities of all substitutions at each position reveals that leucine residues make the largest contributions to activity, followed by the acidic residues (Figure 5A). Similarly, for VP16, aggregating the data by position shows that the key positions are F442, the leucine residues, and the acidic residues (Figure S8A). Acidic and leucine residues make large contributions to activity in these ADs.

The mechanism by which leucine residues make large contributions to activity is exemplified by the structure of the CITED2 interaction with TAZ1. TAZ1 has a canyon with a hydrophobic floor and basic rim that tightly embraces the compact alpha helix of CITED2 (Figure 7B). The leucine residues on CITED2 interact with the hydrophobic canyon floor, and the acidic residues interact with the basic canyon rim. This tight structural constraint explains the activities of many variants. The positions where mutations cause large decreases in activity in Figure 5A point toward the coactivator surface in the NMR structure of CITED2 bound to the TAZ1 domain of CBP/p300 (Figure 5B). Hif1 α showed a similar pattern (Figures 7B and 7C). Replacing leucines with aromatics reduces activity because the larger side chains do not fit in the canyon (Figures 5B and 5E). Disrupting the helix folding by adding two proline residues reduces activity because a helix is very compact and the unfolded peptide likely does not fit (Figures 5B and S9). Adding two glycine residues does not disrupt activity because they do not disrupt the helix formation in simulations and

they are very small (Figure S9). Finally, the D244E substitution reduces activity because the D224 acidic side chain (negative) sits between the narrowest point of the basic canyon rim, sandwiched between the basic (positive) side chains R439 and K365 of TAZ1, and replacing D244 with the larger glutamic acid residue impairs this fit (Figures 5C and S10). Overall, mutations that increase the size of the side chains decrease activity because they impede the helix from fitting into the narrow canyon on TAZ1.

Strong ADs balance hydrophobic and acidic residues

We found that AD activity requires a combination of aromatic and leucine (W,F,Y,L) residues and acidic residues. Plotting the number of W,F,Y,L residues against net charge separates the high- and low-activity variants (Figures 6A and S11A). This separation is less apparent when we count only aromatic residues (Figure S11B) and is somewhat visible when we use calculated Kyte-Doolittle hydrophobicity (Figure S11C). Many points on this grid contain both strong and weak variants (Figure S11A), indicating that composition is not the sole determinant of activity and that the arrangement of residues also matters. We found that composition-based machine learning classifiers could separate the active and inactive variants (Figure S11). When we removed individual parameters from the model, we found that the net charge and leucine residues made the largest contributions to model performance (Table S1). Our results suggest that the balance between W,F,Y,L and acidic residues is critical for AD activity.

Predicting ADs

We examined whether the balance of acidic and W,F,Y,L residues could predict the ADs in human TFs. For one third of human TFs, the only annotated domain is the DBD (Lambert et al., 2018), and only 8% of TFs have an AD annotated in Uniprot (STAR Methods). *In silico*, we broke the protein sequences of 1,608 TFs (Lambert et al., 2018) into exhaustive tiling windows of 39 residues (“tiles”) offset by one amino acid. For each tile, we calculated the net charge and counted the W,F,Y,L residues. We plotted the joint distribution of these properties as a heatmap (Figure 6B, blue) and found that VP16 and CITED2 are on the periphery. Tiles that have both the net charge and hydrophobicity of these ADs are rare—only 0.02% and 0.03% of tiles were as extreme or more extreme than VP16 and CITED2, respectively. Interpolating between these ADs yields 0.13% of tiles ($n = 1,139$, Figure 6B, red), which combine to predict 144 ADs from 136 TFs (Dataset 3). These predicted regions overlap with 17 Uniprot ADs—far more than expected by chance ($p < 1e-5$ in permutation tests). In addition, 11 predicted regions overlap 10 published ADs that are not in Uniprot ($p < 1e-5$ in permutation tests), including the N-terminal AD of c-Myc (Andresen et al., 2012) and the Zn473 KRAB domain (Tycko et al., 2020). The predictor requires the combination of the net negative charge and W,F,Y,L residues because neither property alone provides specific predictions: using only the net charge (-9 from CITED2) yielded 18,086 tiles that combine to 856 predictions, 30 of which overlap the Uniprot ADs; using only the W,F,Y, L counts (7 from VP16) yielded 302,161 tiles that combine to 3,411 predictions, 99 of which overlap the Uniprot ADs. The high degree of overlap between our predicted regions and the literature-validated ADs motivated us to test the predictions experimentally.

Testing the predicted ADs

We tested the predicted regions and found that our composition model accurately predicted the ADs in the human proteome (Figure 6C). In a new experiment, we designed a library with 150 predicted regions (we split long regions to meet synthesis limits), 150 length-matched random regions, and 94 published ADs (STAR Methods). We did not allow the random regions to overlap the predicted regions or Uniprot ADs. We recovered 149 predicted regions, 146 random regions, and 78 published ADs (Data S4). In this dataset, we normalized the three replicates with the No AD control (set to 200 GFP AU). Note that the activity values are not directly comparable with the 5-AD experiment above because the FACS was performed on a different day. When using the No AD TF as the threshold for activity, 108/149 (72%) of the predicted ADs were active, 75/89 (84%) of published ADs were active, and 55/149 (38%) of random regions were active. As a threshold for strong AD activity, we chose the 95th percentile of the random regions (221 AU). At this high threshold, 58/149 (39%) of our predicted regions are strong ADs and 52/89 (58%) of the published ADs are highly active. Although we do not expect all published ADs to work in our assay because some ADs have promoter-specific activities (Goodrich and Tjian, 2010), this analysis demonstrates that our predictor identifies known ADs and accurately predicts previously unidentified ADs.

DISCUSSION

The critical feature of strong ADs is the balance between hydrophobic and acidic residues. Both types of residues are necessary because neither is sufficient alone, and too much of either decreases activity. Hydrophobic residues make critical contacts with coactivators (Dyson and Wright, 2016). Acidic residues can have long-range interactions with basic residues on coactivators (Ferreira et al., 2005; Hermann et al., 2001; Jonker et al., 2005), but these interactions cannot explain the balance requirement. We argue that the balance between hydrophobic and acidic residues can be explained by the acidic exposure model.

In the acidic exposure model, acidic residues and intrinsic disorder keep hydrophobic motifs exposed to solvent where they are available to bind coactivators. Acidic residues prevent local chain compaction through electrostatic repulsion and favorable free energies of solvation. This expansion exposes leucine and aromatic residues to the solvent, so they are available to interact with cofactors. Intrinsic disorder reduces the entropic cost of organizing water around the solvent-exposed hydrophobic residues because fluctuating between the solvent-exposed and the solvent-protected conformations lowers the average cost compared with constant exposure. The acidic exposure model explains why ADs are both negatively charged and intrinsically disordered: the acidic residues and intrinsic disorder combine to keep aromatic and leucine-rich motifs exposed and available to bind coactivators.

Promoting the exposure of hydrophobic motifs is compatible with the other known functions of acidity and disorder in ADs. In specific cases, intramolecular electrostatic interactions between the negatively charged ADs and the positively charged DBDs can increase the DNA binding specificity (Krois et al., 2018; Liu et al., 2008). We speculate that acidic residues may also reduce nonspecific DNA binding by repelling the negatively charged DNA backbone. Intrinsic disorder gives ADs the flexibility to fold into different conformations

when bound to different coactivators (Dyson and Wright, 2016). Intrinsic disorder and acidic residues together can also increase the fraction of molecular collisions that lead to a productive coactivator binding by enabling multiple folding trajectories (Kim et al., 2018; Kim and Chung, 2020). The acidic exposure model is compatible with these biophysical properties of the AD-coactivator interactions.

A key property of ADs is the balance between the strength of their hydrophobic binding motifs and their capacity to keep those motifs exposed to solvent. Adding more hydrophobic residues to ADs will increase their activity so long as their intrinsic disorder and acidic residues can keep the excess hydrophobicity from collapsing the amino acid chain into an inactive conformation. ADs have high hydrophobicity and high acidity, and their activity requires a balance between these two physical properties. We exploited this observation to create an AD predictor that scans for a high but balanced composition of acidity and hydrophobicity. This predictor can be used to prioritize the candidate acidic ADs on poorly characterized TFs in any metazoan genome.

Not all hydrophobic residues make an equal contribution to AD activity. In yeast, aromatic residues make the largest contributions to activity (Erijman et al., 2020; Ravarani et al., 2018; Sanborn et al., 2021; Staller et al., 2018), and, here, we found that in human cells, leucine residues make large contributions to activity. In human cells and yeast, valine and isoleucine (V,I) do not make large contributions to activity, which explains why the choice of hydrophobicity table determines whether AD activity is correlated with hydrophobicity: when we used the Kyte-Doolittle hydrophobicity table, we found no correlation between activity and hydrophobicity because on this table, V and I have large values, whereas W and Y have small values (Kyte and Doolittle, 1982; Staller et al., 2018). By contrast, Sanborn et al. chose the Wimley-White hydrophobicity table which perfectly matches the order of residue contributions to AD activity, leading to a correlation between activity and hydrophobicity (Sanborn et al., 2021; Wimley and White, 1996). These are two among more than 27 published tables, each of which remains an approximation (Colwell et al., 2010). These results further emphasize that I-rich ADs in *Drosophila* are a distinct functional class (Attardi and Tjian, 1993).

There is accumulating evidence that hydrophobic residues in ADs do not always need to be organized into motifs with strict arrangements (sequence grammar). When we designed our mutations, the dominant model was that of the ADs that had motifs surrounded by an acidic context. For example, some ADs contain $\Phi xx\Phi\Phi$ motifs (where Φ is a hydrophobic residue) in an amphipathic alpha helix that presents the hydrophobic residues as a continuous surface to the coactivator, but this is just one solution among many. In yeast, screens of random peptide and extant TFs have failed to find enriched motifs longer than two residues and have shown that some ADs behave as “bags of amino acids” that can be scrambled with a minimal loss of activity (Erijman et al., 2020; Ravarani et al., 2018; Sanborn et al., 2021). For the ADs identified by our predictor, we did not see signatures of grammar. The success of our composition-based predictor, which has no grammar requirement, is evidence for very flexible grammar. We speculate that hydrophobic residues in ADs may simply need to be clustered and not arranged in motifs with specific spacing grammar.

At the same time, we found that within some ADs, there are very strong constraints that reflect the structural constraints of the AD-coactivator interface. Variants that shuffle AD sequences abolish activity, which is evidence for some grammar. Within a hydrophobic motif, the presence of aromatic or leucine residues reflects the structural constraints in the AD-coactivator interaction surfaces, which looks like a strong grammar (Figure 5). Contrasting the CITED2-TAZ1 interaction with the Gcn4-Med15 interaction explains why aromatic residues make large contributions to activity in Gcn4 whereas leucines predominate in CITED2 (Berlow et al., 2017; Brzovic et al., 2011). Both ADs fold into alpha helices, and both coactivators contain a binding canyon with a hydrophobic floor and basic rim (Figure 7A). On TAZ1, the canyon is large and the CITED2 alpha helix is engulfed (Figure 7B). Leucines fit this structure better than aromatics because they are smaller and promote folding into a compact helix (Pace and Scholtz, 1998). On Med15, the canyon is shallow and Gcn4 only inserts side chains. A recent structure of the Gal4-Med15 binding interaction shows a similar fuzzy interaction centered on aromatic and leucine residues (Pacheco et al., 2018; Tuttle et al., 2021). Aromatics fit the Med15 binding surface better than leucine residues because they more easily reach the hydrophobic canyon floor. The increased importance of leucine residues in human ADs, such as CITED2, likely reflects the structural constraints imposed by an expanded repertoire of coactivators. Going forward, new approaches to high-throughput mutagenesis will be efficient for exploring the structural constraints of the protein-protein interaction surfaces (Diss and Lehner, 2018; Rollins et al., 2019; Schmiedel and Lehner, 2019).

The acidic exposure model can explain several results in the literature. Screens of random peptides found enrichment of [DE][WFY] “mini motifs,” which support our model (Erijman et al., 2020; Ravarani et al., 2018; Sanborn et al. 2021). Sanborn et al. examined synthetic 9-mer peptides that mixed aromatic and D residues and observed an increase and decrease in activity as aromatics are added (Sanborn et al., 2021). Peak activity occurs when the D’s and F’s are well-mixed or when the F’s are on the C terminus of the TF, both of which promote F exposure and activity. Sanborn et al. screened the ability of diverse sequences to modulate the activity of the Pdr1 AD and found that hydrophobic residues decrease activity and acidic residues boost activity. This modulation is consistent with hydrophobic residues promoting collapse and acidic residues promoting exposure. Balanced sequences are the most active.

We synthesize our findings in three conclusions: (1) strong acidic ADs balance hydrophobic motifs and acidic residues; (2) clusters of W,F,Y,L residues surrounded by acidic residues are sufficient to predict new ADs; (3) the choice between aromatic and leucine residues in an acidic AD is constrained by the structure of the coactivator interaction surface. These rules apply to a subset of traditional acidic ADs, and our work implies that there are multiple subclasses of acidic ADs. These insights will help refine computational models for predicting ADs, guide engineering of ADs, and inform of the models that predict the impact of genetic variation on AD function.

STAR★METHODS

RESOURCE AVAILABILITY

Lead contact—Further information and requests for resources and reagents should be directed to Barak A. Cohen, cohen@wustl.edu

Materials availability—The plasmids generated in this study have been deposited at AddGene.

The cell lines generated in this study are available upon request.

Data and code availability

- The AD activity data are included as Data S1, S2, and S4. The Illumina sequencing data have been deposited at GEO and are publicly available as of the date of publication. Accession numbers are listed in the key resources table. All simulation data and flow cytometry data reported in this paper will be shared by the lead contact upon request.
- The analysis code has been deposited in a public Github repository with a Zenodo DOI listed in the key resources table.
- Any additional information required to reanalyze the data reported in this paper is available from the lead contact upon request.

EXPERIMENTAL MODEL AND SUBJECT DETAILS

Cell line construction—To engineer the K562 cell line we began with LP3 from (Maricque et al., 2018). These female cells were authenticated in Maricque et al. (2018) just before we started using them. This landing pad is located on chromosome 11. First, we introduced a frameshift mutation to the GFP in the landing pad using Cas9 (from Shondra Miller, Washington University School of Medicine GeiC) and a gRNA against GFP (AddGene 41819). Second, we integrated our reporter at the AAVS1 locus using Cas9, the SM58 SSB2 T2 gRNA (from Shondra Miller) and the pMVS184 reporter plasmid. Starting on Day 2, we selected for integrations with 1 ug/ml puromycin for three days. We tested candidate reporter clones with transfections of a synthetic TF (pMVS 223) carrying p53 AD1, choosing the clone with the largest dynamic range between baseline GFP and the brightest transfected cells. Our internal name for this clone is T7.1E3.

Cells were grown in Iscove's Modified Dulbecco's Medium (IMDM) medium +10% FBS +1% Non Essential Amino Acids +1% PennStrep (Gibco). All transfections used the Invitrogen Neon electroporation machine using a 100 ul tip, 1.2 M cells and 5 ug of DNA.

METHOD DETAILS

Rational mutagenesis—The sequences of all 525 VP16, Hif1 α , CITED2, Stat3 and p65 variants are listed in Data S1. The systematic mutagenesis added and removed charged residues or aromatic residues. Net charge of ADs was changed in two ways: subsets of charged residues were changed to each of the four charged residues and alanine, or subsets

of polar residues were changed to charged residues. Aromatic residues were changed to alanine, leucine or other aromatic residues, and aromatic residues were added by replacing leucine, isoleucine, alanine, methionine, and valine residues.

The “Hand Designed” p53 AD variants contained the same systematic mutations and more hand designed variants listed in Data S2. The p53 mutagenesis also included a deep mutational scan, a double alanine scan and sequences from orthologous TFs. Activity values of each dataset are normalized separately and should not be directly compared.

Plasmid library construction—The plasmid sequences for the GFP reporter (pMVS184, Addgene 176294) and synthetic TF chassis (pMVS223, Addgene 176293) are in Data S8.

In the 5 AD library, we designed the AD variants as protein sequences and reverse translated using optimal human codons. We attached each variant to 28 unique 12 bp FREE barcodes (Hawkins et al., 2018). WT ADs had 84 barcodes each. Between the AD and the barcode are BamHI, SacI and NheI restriction sites. For ADs that were less than 46AA, we added random filler DNA between the BamHI and SacI sites. We added PCR primers at the start (CCCAGCTTAAGCCACCATG) and end (CTCGAGATAACTTCGTATAATGTATGCTAT). Note there is an XhoI site after the barcode, included in the downstream primer. We ordered 14968 unique 217 bp ssDNA oligos from Agilent.

We cloned the AD variant library by HiFi assembly. We added plasmid homology to the ssDNA oligos by PCR, yielding a 232 bp product, with 4 cycles, Q5 polymerase, 0.5 pmol template and 8 reactions. The cloning primers were: TCACCGACCTCTCTCCCCAGCTTAAGCCACCATG and ATAGCATACATTATACGAAGTTATCTCGAG. We digested the pMVS223 backbone with AflII, XhoI and KpnI-HF and gel purified it. Each assembly had 100 ng of backbone and 5x molar ratio of insert. We electroporated bacteria and collected ~20 million colonies. We checked the library with paired end Illumina sequencing. We recovered 98.7% of our barcodes and all AD variants. For the second step of library cloning, we digested the library and pMVS223 with BamHI-HF and NheI-HF, and inserted the synthetic TF by T4 ligation. We electroporated bacteria and collected 400K colonies. We recovered 93% of designed barcodes and all ADs. In the final plasmid library the ADs are on the N terminus of the protein, between the initial methionine (ATG start) and a GSGS linker. In the No AD control there is nothing between the starting methionine and the GSGS linker. The synthetic TF is followed by a P2A cleavage sequence and an in frame Neomycin resistance gene. As a result, 1 and 2 bp deletions, the most common oligo synthesis errors, lead to frameshifts and are selected against after the library is integrated into the genome.

The p53 library was constructed in the same way with 5 barcodes per variant, 30 for WT AD1 and 25 for WT AD2. We collected 4 million colonies after step one and 26 million after step two. We recovered 14355 of 14998 designed barcodes and 2990 of 2991 designed ADs. In this work we used data from both WT ADs and 171 hand designed variants.

All restriction enzymes, HiFi mix, and competent bacteria were purchased from NEB. Library Maxipreps were performed using the ZymoPURE II Plasmid Maxiprep Kit (Zymo).

Plasmid library integration and measurement—In each transfection, we used 1.2 M cells, 2 ug of CMV-Cre (Maricque et al., 2018) and 3 ug of Plasmid Library. We transfected 102 M cells in 86 transfections split into 22 flasks. The next day, we began selection with 400 ng/ml G418 for 10 days. On Day 11 we performed magnetic enrichment of live cells (MACS by Miltenyi Biotec). We combined flasks 1–5 into biological replicate 1, flasks 6–10 into biological replicate 2, flasks 11–15 into biological replicate 3, and flasks 16–22 into biological replicate 4. On Day 12, we added β -estradiol to a final concentration of 1 μ M.

On Day 15 we sorted cells on a Sony HAPS 2 at the Siteman Cancer Center Flow Cytometry Core. We set an ON/OFF threshold for GFP as the 90th percentile of the uninduced population (Figure S12). The lowest bin was the bottom 50% of the OFF population. The ON region was split into 3 bins with equal populations. For each replicate, we collected 750K cells in each of the four bins. We noted the median fluorescence of each bin and used that number to calculate AD activity (see below). The dynamic range of the measurement is determined by the fluorescence values of the dimmest and brightest bin (Table S2). After collecting the 4 independent replicates, we combined all the cells and sorted them into 8 bins each with ~12% of the population—this sample has a larger dynamic range (Table S2). These values are included in Data S1. These values are well correlated with the mean of the four biological replicates, but because it is a single measurement, it does not have error bars. In the figures we plotted the mean and standard deviation of the 4 biological replicates.

Barcode amplicon sequencing libraries—Genomic DNA was collected using the Qiamp DNA Mini kit (Qiagen). We performed 8 PCRs on each sample. The sequencing libraries were prepared in 2 batches: Batch 1 contained biological replicates 1–3 and Batch 2 contained biological replicate 4 and the 8 bin sort. We did 25 cycles with NEB Q5 polymerase using CP36.P10 and LP_019 primers. We pooled the PCRs, cleaned up the DNA (NEB Monarch), quantified it, digested the entire sample with NheI and EcoRI-HF (NEB) for 90 minutes and then ligated sequencing adaptors with T4 ligase (NEB) for 30 min. These adaptors contained sample barcodes in Read1 and Index1 We used 4 ng of this ligation for a 20 cycle enrichment PCR with Q5 and the EPCR_P1_short and EPCR_PE2_short primers. We sequenced each Batch on a NextSeq 500 1 \times 75 High Output run.

Each biological p53 replicate was sorted on a different day, so each sequencing library was sequenced separately with a NextSeq 500 1 \times 75 High Output run.

CP36.P10 ctcccgattcgagcgcac

LP_019 GCAGCGTATCCACATAGCGTAAAAG

EPCR_P1_short AATGATACGGCGACCACCGAG

EPCR_PE2_short CAAGCAGAAGACGGCATAACGAGAT

To assess the number of integrations in each experiment, we saved 1 ml of culture (0.5–1M cells) from each flask (4 transfections) before the magnetic enrichment for live cells (Day 11). We extracted gDNA, amplified barcodes, and sequenced. We identified 96,000 unique integrations, an underestimate. In the sorted samples we recovered 14015 barcodes (93.6%

of designed) total, 7164 in all four replicates and 10798 in three or more replicates. All ADs were present in all replicates.

QUANTIFICATION AND STATISTICAL ANALYSIS

Data processing—We demultiplexed samples using a combination of Index 1 reads and Read1 inline barcodes using the ‘fastqconvert_XbaI.py.’ We identified barcodes (grep), sorted the barcodes (sort) and counted them (unique -c) with the ‘processMSS18_Sort4_5_LigAdaptors.sh’ scripts. Demultiplexed fastq files have been deposited in GEO.

Using perfect matches, we counted the abundance of each FREE barcode in each sample using the ‘Preprocessing_MSS18_MergeBCs_NextSeq_p53_2021_forpublication.ipynb’ script. We normalized the read counts first by the total reads in each sample and then renormalized each barcode across bins to create a probability mass function. We used the probability mass function and the median GFP fluorescence of each bin (Table S2) to calculate the activity of each barcode. To remove outlier barcodes, we found all barcodes for an AD, computed the activity of each barcode, computed the mean and variance of the set of barcodes and then removed any barcodes whose activity was more than two standard deviations away from the mean. We then took all the reads from all remaining barcodes, pooled them and recomputed activity. This approach led to one activity measurement for each AD in each biological replicate. The maps between AD sequences and DNA barcodes are included in Data S5, S6 and S7.

To combine data across replicates we used the ‘No AD control.’ We thank an anonymous reviewer for inspiring this analysis. In our library cloning, the parent plasmid (pMVS223), which does not carry an AD, is present a low background, and this plasmid carries a unique 9 bp barcode. We computed the activity of this No AD control in each replicate. Next we adjusted the raw activity values (by addition or subtraction) so that the No AD control had an activity of 2000 in each replicate. We chose 2000 so that no activity values would be negative. We used the average and standard deviations of these adjusted activity values for further analysis.

For the p53 data, each replicate was collected on a different day using 2 sorters (Replicate 1 and 3: Sony HAPS 2; Replicate 2: a highly modified Beckman Coulter MoFlow). Replicates 1 and 2 were sorted into 4 bins; Replicate 3 was sorted into 8 bins). To combine these data we converted activities into Z scores and computed the mean and standard error of the mean (SEM). The p53 control variants are from (Chang et al., 1995; Lin et al., 1994).

In the next step of preprocessing, we added physical property calculations and AD sequence names to the activity data using the ‘MSS18 Step 2 of Preprocessing (fix names and add columns) For publication.ipynb’. This script also manually corrected errors in sequence names.

Analysis—All analysis was performed in Jupyter Notebooks with python 2.7 and Matplotlib, seaborn, pandas, localcider, biopython, logomaker (Tareen and Kinney, 2020), scipy, statsmodels, sklearn, and itertools. Colors are from Colorbrewer ([https://](https://colorbrewer2.org/)

colorbrewer2.org/). AD sequence properties were calculated with localcider (Holehouse et al., 2017). To identify AD variants that were statistically significantly different from each WT, we used a two-sided t test and 5% FDR correction. We computed the regressions with statsmodels.api.OLS.

Structures were downloaded from the RSCB PDB (www.rcsb.org) and visualized with VMD (Humphrey et al., 1996). We normalized activity values to [0–1], mapped the values to the Beta column of the pdb file and visualized positions with normalized activity < 0.2 (Figure 5B and S8C).

To summarize the effects of substitutions at each position (Figures 5A and S8A,B), we identified all variants that changed each position, collected the activity measurements from all biological replicates and created a boxplot. We excluded the shuffle variants.

Sequence properties were calculated with the localcider package or by counting amino acids. The Omega parameter was computed with localcider using the `get_kappa_X(['W','F','Y','L'],['D','E'])` command.

Figure panels were generated with the 'MSS18 PaperFiguresRevision.ipynb' and 'MSS19_predictedADs_forpublication_v2.ipynb' jupyter notebooks in the Github repository.

Machine learning—The machine learning analysis was carried out in python with the sklearn package. We started with all variants of VP16, Hif1 α and CITED2 and then excluded the shuffle variants. The High Activity set (N = 121) had variants with a mean activity above 3400. The Low Activity set (N = 134) had variants with a mean activity below 2900 (Figure S11F). We normalized all parameters to be between [0,1]. We performed 5-fold cross validation and assessed model performance with the Area Under the Curve (AUC) of the Receiver Operator Characteristic (ROC). We compared Support Vector Machines, Logistic Regression and Random Forest classifiers.

All atom simulations—We ran all-atom, Monte Carlo simulations in the CAMPARI simulation engine (campari.sourceforge.net) using the ABSINTH implicit solvent paradigm (Vitalis and Pappu, 2009). This simulation framework is a well established approach to study the conformational ensembles of intrinsically disordered regions (Martin et al., 2016; Metskas and Rhoades, 2015; Vitalis and Pappu, 2009) and we have previously used it to study the Central Acidic AD of the yeast TF, Gcn4 (Staller et al., 2018). We simulated all VP16 and CITED2 variants. For Hif1 α , we simulated all hand designed variants and the WT sequence.

For each variant, we ran ten simulations starting in a helix and ten starting in a random coil. For the WT sequences, we ran 30 simulations from each starting configuration. In total we ran 4300 simulations. Each simulation had a pre-equilibration run of 2M steps. Then we began the main simulation with 10M steps of equilibration and the main simulation of 50M steps, extracting the conformation every 10K steps, yielding 5000 conformations per simulation. Simulation analysis was performed with the CAMPARItraj (ctraj.com), now SOURSOP (<https://soursop.readthedocs.io/>), software suite. This software

suite calculated helicity with the DSSP algorithm (Kabsch and Sander, 1983) and radius of gyration as the distribution of atoms in each confirmation without weighting by mass (Holehouse et al., 2017). The accessibility was calculated by rolling a 1.5 nm spherical marble around each confirmation and summing the solvent accessible surface area of the W,F,Y,L residues (Staller et al., 2018). To speed up this analysis accessibility was assessed every 20 confirmations.

The summary statistics for all the simulations is in Data S9.

Predicting ADs in human TFs—We downloaded protein sequences from Uniprot for 1608 TFs (Lambert et al., 2018). For each TF, we created 39 AA tiling windows, spaced every 1 AA, yielding 881,344 tiles. For each tile, we computed the net charge (counting D,E,K&R) and counted W,F,Y,L residues.

We identified tiles that were as extreme or more extreme than VP16 and CITED2. We used a diagonal line to extrapolate between these ADs. The tiles predicted to cover ADs (Figure 6B, red pixels), fulfill 3 criteria:

$$(\text{Charge} < -9) \text{ AND } (\text{WFYL} > 7) \text{ AND } (((\text{Charge} + 9) - (\text{WFYL} - 10)) < = 0)$$

This algorithm identified 1139 tiles, 0.129% of the total. We aggregated overlapping tiles to predict 144 ADs on 136 TFs (See Data S3 for locations on parent TFs and sequences). To test these predictions, we used ADs annotated in Uniprot. We downloaded.gff files for the 1608 TFs from Uniprot. We used 4 regular expressions to search the “regions” column of the.gff files for “activation”, “TAD”, “Required for transcriptional activation” and “Required for transcriptional activation.” These searches yielded 110 unique ADs, including 7 proline rich ADs (>20% proline) and 3 glutamine rich ADs (>20% glutamine).

We used permutation tests to determine if our predictor was better than random. We randomly selected 136 TFs, randomly selected 144 length matched regions and determined how many overlapped the 110 known ADs. For the 4 TFs with 2 predicted ADs, we preserved the coupling between these lengths. In 100K permutations, we never observed more than 11 overlaps. 17 of our predicted ADs overlapped the 110 Uniprot ADs.

Testing predicted ADs—We built a third plasmid library to test the predicted ADs. Due to DNA synthesis limits, we split long predicted regions and tested 150 regions of 39–76 residues. To create an empirical distribution for the prevalence of ADs on TFs, we included 150 length-matched regions randomly drawn from TF sequences (Lambert et al., 2018). We required that these random regions did not overlap our predicted ADs or Uniprot ADs. The 92 positive control ADs were drawn from: 36 hand-curated ADs (RegionType=Hand_Curated_ADs), 35 ADs from a published list (RegionType=Choi_2000_PMIID_10821850) (Choi et al., 2000), 19 Uniprot domains that overlapped our predictions (RegionType=Uniprot), and 2 published synthetic DW or DF runs (RegionType=Controls) (Ravarani et al., 2018). We also included 3 KRAB domains from Uniprot, 22 mutant ADs and 26 regions tiling the human TF, Crx. Due to human error, we did not test the correct predicted region of AEBP1 (Q8IUX7) and tested 2 other regions

instead. The full list of sequences and activities is included in Data S4. The ‘Known ADs’ in Figure 6C are flagged in the ‘Positive Controls’ column. The ‘Negative Controls’ column indicates mutant ADs.

The plasmid library was cloned in a similar manner as above. The oligos were ordered as a oPool from IDT. Oligo length varied. For each AD, we included one 9 bp ‘AD barcode’ (Hawkins et al., 2018). During the second step of cloning, we added 6 Ns downstream of the synthetic TF by PCR, which became the ‘integration barcode.’ In principle, a different integration barcode marks each plasmid integration event, analogous to a Unique Molecular Identifier in single cell RNA-seq protocols. The resulting ‘composite barcode’ contained a 6 bp ‘integration barcode’, the NheI restriction site and the 9 bp ‘AD barcode.’ 76 transfections were split into 3 biological replicates. G418 selection began on Day 1, magnetic separation was performed on Day 11, β -estradiol induction began on Day 11 and cell sorting on Day 14. For each biological replicate, we sorted into 4 bins. During the sequencing library preparation, we performed 24 PCRs for each gDNA sample. We added Index1 and Index2 barcodes by PCR.

After integrating the plasmid library into cells, we deeply sequenced gDNA from the unsorted cell pool to build a ‘composite barcode’ table (Check_Complexity_MSS19_nextSeq.ipynb). This table contained 44077 composite barcodes with at least 10 reads in one of the 3 biological replicates. For all subsequent analysis, we matched reads to this table. We used perfect matches to designed ‘AD barcodes’ and combined reads for all ‘integration barcodes’ attached to each ‘AD barcode’ as described above: we first removed outliers and then combined read counts (MSS19_preprocessing.ipynb). In this experiment, we found that the No AD Control TF had 9, 10, 10 integration barcodes in each replicate, respectively. We combined replicates by first setting the activity of the No AD Control to 200 and then computing the mean and standard deviation. The biological replicates contained 20850, 19758 and 21656 uniquely identifiable integrations. We designed 443 ADs, detected 434 in the plasmid library, and detected 431 integrated into cells. We required 5 or more unique integration barcodes in at least one replicate, yielding 428 ADs for downstream analysis. In Figure 6C, the threshold for AD activity was 200, and the threshold for strong AD activity was 223, the 95th percentile of the random regions.

Supplementary Material

Refer to Web version on PubMed Central for supplementary material.

ACKNOWLEDGMENTS

We thank Minhee Park and Ahmed Khalil for sharing the synthetic DBD and promoter sequence ahead of publication; Kiersten Ruff, Avi Ramu, and Nicole Rockweiler for bioinformatics help; Brittany Pioso for their help with the cartoons; Jessica Hoisington-Lopez and MariaLynn Crosby for DNA sequencing. We thank members of the Cohen Lab and Thomas Graham for helpful discussions and comments on the manuscript. M.V.S. was supported by the Burroughs Wellcome Fund Postdoctoral Enrichment Program, American Cancer Society Postdoctoral Fellowship, NIGMS K99131022, and NSF 2112057. E.R. was supported by the McDonnell Genome Institute Opportunities in Genomics Research Program under grant NIH-R25HG006687. This work was supported by grants from the National Institutes of Health, NINDS 5R01NS056114 to R.V.P., NIGMS R01GM092910 to B.A.C., and the Children’s Discovery Institute CDI-LI-2018-765 to B.A.C.

REFERENCES

- Andresen C, Helander S, Lemak A, Farès C, Csizmok V, Carlsson J, Penn LZ, Forman-Kay JD, Arrowsmith CH, Lundström P, and Sunnerhagen M (2012). Transient structure and dynamics in the disordered c-Myc transactivation domain affect Bin1 binding. *Nucleic Acids Res.* 40, 6353–6366. [PubMed: 22457068]
- Attardi LD, and Tjian R (1993). *Drosophila* tissue-specific transcription factor NTF-1 contains a novel isoleucine-rich activation motif. *Genes Dev.* 7, 1341–1353. [PubMed: 8330738]
- Berlow RB, Dyson HJ, and Wright PE (2017). Hypersensitive termination of the hypoxic response by a disordered protein switch. *Nature* 543, 447–451. [PubMed: 28273070]
- Brady CA, Jiang D, Mello SS, Johnson TM, Jarvis LA, Kozak MM, Kenzelmann Broz D, Basak S, Park EJ, McLaughlin ME, et al. (2011). Distinct p53 transcriptional programs dictate acute DNA-damage responses and tumor suppression. *Cell* 145, 571–583. [PubMed: 21565614]
- Brzovic PS, Heikaus CC, Kisselev L, Vernon R, Herbig E, Pacheco D, Warfield L, Littlefield P, Baker D, Klevit RE, and Hahn S (2011). The acidic transcription activator Gcn4 binds the mediator subunit Gal11/Med15 using a simple protein interface forming a fuzzy complex. *Mol. Cell* 44, 942–953. [PubMed: 22195967]
- Chang J, Kim DH, Lee SW, Choi KY, and Sung YC (1995). Transactivation ability of p53 transcriptional activation domain is directly related to the binding affinity to TATA-binding protein. *J. Biol. Chem.* 270, 25014–25019. [PubMed: 7559631]
- Choi Y, Asada S, and Uesugi M (2000). Divergent hTAFII31-binding motifs hidden in activation domains. *J. Biol. Chem.* 275, 15912–15916. [PubMed: 10821850]
- Colwell LJ, Brenner MP, and Ribbeck K (2010). Charge as a selection criterion for translocation through the nuclear pore complex. *PLoS Comput. Biol.* 6, e1000747. [PubMed: 20421988]
- Cress WD, and Triezenberg SJ (1991). Critical structural elements of the VP16 transcriptional activation domain. *Science* 251, 87–90. [PubMed: 1846049]
- Currie SL, Doane JJ, Evans KS, Bhachech N, Madison BJ, Lau DKW, McIntosh LP, Skalicky JJ, Clark KA, and Graves BJ (2017). ETV4 and AP1 transcription factors form multivalent interactions with three sites on the MED25 activator-interacting domain. *J. Mol. Biol.* 429, 2975–2995. [PubMed: 28728983]
- Diss G, and Lehner B (2018). The genetic landscape of a physical interaction. *eLife* 7, e32472. [PubMed: 29638215]
- Dyson HJ, and Wright PE (2016). Role of intrinsic protein disorder in the function and interactions of the transcriptional coactivators CREB-binding protein (CBP) and p300. *J. Biol. Chem.* 291, 6714–6722. [PubMed: 26851278]
- El-Gebali S, Mistry J, Bateman A, Eddy SR, Luciani A, Potter SC, Qureshi M, Richardson LJ, Salazar GA, Smart A, et al. (2019). The Pfam protein families database in 2019. *Nucleic Acids Res* 47, D427–D432. [PubMed: 30357350]
- Erijman A, Kozłowski L, Sohrabi-Jahromi S, Fishburn J, Warfield L, Schreiber J, Noble WS, Söding J, and Hahn S (2020). A high-throughput screen for transcription activation domains reveals their sequence features and permits prediction by deep learning. *Mol. Cell* 78, 890–902.e6. [PubMed: 32416068]
- Ferreira ME, Hermann S, Prochasson P, Workman JL, Berndt KD, and Wright APH (2005). Mechanism of transcription factor recruitment by acidic activators. *J. Biol. Chem.* 280, 21779–21784. [PubMed: 15826952]
- Finn RD, Coggill P, Eberhardt RY, Eddy SR, Mistry J, Mitchell AL, Potter SC, Punta M, Qureshi M, Sangrador-Vegas A, et al. (2016). The Pfam protein families database: towards a more sustainable future. *Nucleic Acids Res* 44, D279–D285. [PubMed: 26673716]
- Freedman SJ, Sun Z-YJ, Kung AL, France DS, Wagner G, and Eck MJ (2003). Structural basis for negative regulation of hypoxia-inducible factor-1 α by CITED2. *Nat. Struct. Biol.* 10, 504–512. [PubMed: 12778114]
- Giacomelli AO, Yang X, Lintner RE, McFarland JM, DUBY M, Kim J, Howard TP, Takeda DY, Ly SH, Kim E, et al. (2018). Mutational processes shape the landscape of TP53 mutations in human cancer. *Nat. Genet.* 50, 1381–1387. [PubMed: 30224644]

- Goodrich JA, and Tjian R (2010). Unexpected roles for core promoter recognition factors in cell-type-specific transcription and gene regulation. *Nat. Rev. Genet.* 11, 549–558. [PubMed: 20628347]
- Gray VE, Hause RJ, and Fowler DM (2017). Analysis of large-scale mutagenesis data to assess the impact of single amino acid substitutions. *Genetics* 207, 53–61. [PubMed: 28751422]
- Hawkins JA, Jones SK Jr., Finkelstein IJ, and Press WH (2018). Indel-correcting DNA barcodes for high-throughput sequencing. *Proc. Natl. Acad. Sci. USA* 115, E6217–E6226. [PubMed: 29925596]
- Hermann S, Berndt KD, and Wright AP (2001). How transcriptional activators bind target proteins. *J. Biol. Chem.* 276, 40127–40132. [PubMed: 11514548]
- Holehouse AS, Das RK, Ahad JN, Richardson MOG, and Pappu RV (2017). CIDER: resources to analyze sequence-ensemble relationships of intrinsically disordered proteins. *Biophys. J.* 112, 16–21. [PubMed: 28076807]
- Humphrey W, Dalke A, and Schulten K (1996). VMD: visual molecular dynamics. *J. Mol. Graph.* 14, 33–38. [PubMed: 8744570]
- Jackson BM, Drysdale CM, Natarajan K, and Hinnebusch AG (1996). Identification of seven hydrophobic clusters in GCN4 making redundant contributions to transcriptional activation. *Mol. Cell. Biol.* 16, 5557–5571. [PubMed: 8816468]
- Jonker HRA, Wechselberger RW, Boelens R, Folkers GE, and Kaptein R (2005). Structural properties of the promiscuous VP16 activation domain. *Biochemistry* 44, 827–839. [PubMed: 15654739]
- Kabsch W, and Sander C (1983). Dictionary of protein secondary structure: pattern recognition of hydrogen-bonded and geometrical features. *Biopolymers* 22, 2577–2637. [PubMed: 6667333]
- Kim J-Y, and Chung HS (2020). Disordered proteins follow diverse transition paths as they fold and bind to a partner. *Science* 368, 1253–1257. [PubMed: 32527832]
- Kim J-Y, Meng F, Yoo J, and Chung HS (2018). Diffusion-limited association of disordered protein by non-native electrostatic interactions. *Nat. Commun.* 9, 4707. [PubMed: 30413699]
- Kinney JB, Murugan A, Callan CG Jr., and Cox EC (2010). Using deep sequencing to characterize the biophysical mechanism of a transcriptional regulatory sequence. *Proc. Natl. Acad. Sci. USA* 107, 9158–9163. [PubMed: 20439748]
- Krois AS, Dyson HJ, and Wright PE (2018). Long-range regulation of p53 DNA binding by its intrinsically disordered N-terminal transactivation domain. *Proc. Natl. Acad. Sci. USA* 115, E11302–E11310. [PubMed: 30420502]
- Kyte J, and Doolittle RF (1982). A simple method for displaying the hydropathic character of a protein. *J. Mol. Biol.* 157, 105–132. [PubMed: 7108955]
- Lambert SA, Jolma A, Campitelli LF, Das PK, Yin Y, Albu M, Chen X, Taipale J, Hughes TR, and Weirauch MT (2018). The human transcription factors. *Cell* 175, 598–599. [PubMed: 30290144]
- Latchman DS (2008). *Eukaryotic Transcription Factors* (Elsevier Science).
- Lecoq L, Raiola L, Chabot PR, Cyr N, Arseneault G, Legault P, and Omichinski JG (2017). Structural characterization of interactions between transactivation domain 1 of the p65 subunit of NF- κ B and transcription regulatory factors. *Nucleic Acids Res* 45, 5564–5576. [PubMed: 28334776]
- Lin J, Chen J, Elenbaas B, and Levine AJ (1994). Several hydrophobic amino acids in the p53 amino-terminal domain are required for transcriptional activation, binding to mdm-2 and the adenovirus 5 E1B 55-kD protein. *Genes Dev* 8, 1235–1246. [PubMed: 7926727]
- Liu Y, Matthews KS, and Bondos SE (2008). Multiple intrinsically disordered sequences alter DNA binding by the homeodomain of the Drosophila hox protein ultrabithorax. *J. Biol. Chem.* 283, 20874–20887. [PubMed: 18508761]
- Mago T, and Salzberg SL (2011). FLASH: fast length adjustment of short reads to improve genome assemblies. *Bioinformatics* 27, 2957–2963. [PubMed: 21903629]
- Majithia AR, Tsuda B, Agostini M, Gnanapradeepan K, Rice R, Peloso G, Patel KA, Zhang X, Broekema MF, Patterson N, et al. (2016). Prospective functional classification of all possible missense variants in PPAR γ . *Nat. Genet.* 48, 1570–1575. [PubMed: 27749844]
- Maricque BB, Chaudhari HG, and Cohen BA (2018). A massively parallel reporter assay dissects the influence of chromatin structure on cis-regulatory activity. *Nat. Biotechnol.* 19, 2018. Published online November. 10.1038/nbt.4285.

- Martin EW, Holehouse AS, Grace CR, Hughes A, Pappu RV, and Mittag T (2016). Sequence determinants of the conformational properties of an intrinsically disordered protein prior to and upon multisite phosphorylation. *J. Am. Chem. Soc.* 138, 15323–15335. [PubMed: 27807972]
- McIsaac RS, Oakes BL, Wang X, Dummit KA, Botstein D, and Noyes MB (2013). Synthetic gene expression perturbation systems with rapid, tunable, single-gene specificity in yeast. *Nucleic Acids Res* 41, e57. [PubMed: 23275543]
- Metskas LA, and Rhoades E (2015). Conformation and dynamics of the troponin I C-terminal domain: combining single-molecule and computational approaches for a disordered protein region. *J. Am. Chem. Soc.* 137, 11962–11969. [PubMed: 26327565]
- Pace CN, and Scholtz JM (1998). A helix propensity scale based on experimental studies of peptides and proteins. *Biophys. J.* 75, 422–427. [PubMed: 9649402]
- Pacheco D, Warfield L, Brajcich M, Robbins H, Luo J, Ranish J, and Hahn S (2018). Transcription activation domains of the yeast factors Met4 and Ino2: tandem activation domains with properties similar to the yeast Gcn4 activator. *Mol. Cell. Biol.* 38, e00038–18. [PubMed: 29507182]
- Park M, Patel N, Keung AJ, and Khalil AS (2019). Engineering epigenetic regulation using synthetic read-write modules. *Cell* 176, 227–238.e20. [PubMed: 30528434]
- Raj N, and Attardi LD (2017). The transactivation domains of the p53 protein. *Cold Spring Harb. Perspect. Med.* 7, a026047. [PubMed: 27864306]
- Ravarani CN, Erkina TY, De Baets G, Dudman DC, Erkin AM, and Babu MM (2018). High-throughput discovery of functional disordered regions: investigation of transactivation domains. *Mol. Syst. Biol.* 14, e8190. [PubMed: 29759983]
- Regier JL, Shen F, and Triezenberg SJ (1993). Pattern of aromatic and hydrophobic amino acids critical for one of two subdomains of the VP16 transcriptional activator. *Proc. Natl. Acad. Sci. USA* 90, 883–887. [PubMed: 8381535]
- Rollins NJ, Brock KP, Poelwijk FJ, Stiffler MA, Gauthier NP, Sander C, and Marks DS (2019). Inferring protein 3D structure from deep mutation scans. *Nat. Genet.* 51, 1170–1176. [PubMed: 31209393]
- Sanborn AL, Yeh BT, Feigerle JT, Hao CV, Townshend RJ, Lieberman Aiden E, Dror RO, and Kornberg RD (2021). Simple biochemical features underlie transcriptional activation domain diversity and dynamic, fuzzy binding to mediator. *eLife* 10, e68068. [PubMed: 33904398]
- Schmiedel JM, and Lehner B (2019). Determining protein structures using deep mutagenesis. *Nat. Genet.* 51, 1177–1186. [PubMed: 31209395]
- Sharon E, Kalma Y, Sharp A, Raveh-Sadka T, Levo M, Zeevi D, Keren L, Yakhini Z, Weinberger A, and Segal E (2012). Inferring gene regulatory logic from high-throughput measurements of thousands of systematically designed promoters. *Nat. Biotechnol.* 30, 521–530. [PubMed: 22609971]
- Shen F, Triezenberg SJ, Hensley P, Porter D, and Knutson JR (1996a). Transcriptional activation domain of the herpesvirus protein VP16 becomes conformationally constrained upon interaction with basal transcription factors. *J. Biol. Chem.* 271, 4827–4837. [PubMed: 8617752]
- Shen F, Triezenberg SJ, Hensley P, Porter D, and Knutson JR (1996b). Critical amino acids in the transcriptional activation domain of the herpesvirus protein VP16 are solvent-exposed in highly mobile protein segments. An intrinsic fluorescence study. *J. Biol. Chem.* 271, 4819–4826. [PubMed: 8617751]
- Staller MV, Holehouse AS, Swain-Lenz D, Das RK, Pappu RV, and Cohen BA (2018). A high-throughput mutational scan of an intrinsically disordered acidic transcriptional activation domain. *Cell Syst* 6, 444–455.e6. [PubMed: 29525204]
- Tareen A, and Kinney JB (2020). Logomaker: beautiful sequence logos in Python. *Bioinformatics* 36, 2272–2274. [PubMed: 31821414]
- Tuttle LM, Pacheco D, Warfield L, Wilburn DB, Hahn S, and Klevit RE (2021). Mediator subunit Med15 dictates the conserved “fuzzy” binding mechanism of yeast transcription activators Gal4 and Gcn4. *Nat. Commun.* 12, 2220. [PubMed: 33850123]
- Tycko J, DelRosso N, Hess GT, Aradhana, Banerjee A, Mukund A, Van MV, Ego BK, Yao D, Spees K, et al. (2020). High-throughput discovery and characterization of human transcriptional effectors. *Cell* 183, 2020–2035.e16. [PubMed: 33326746]

- Vitalis A, and Pappu RV (2009). ABSINTH: a new continuum solvation model for simulations of polypeptides in aqueous solutions. *J. Comput. Chem.* 30, 673–699. [PubMed: 18506808]
- Vogel TP, Milner JD, and Cooper MA (2015). The Ying and Yang of STAT3 in human disease. *J. Clin. Immunol.* 35, 615–623. [PubMed: 26280891]
- Warfield L, Tuttle LM, Pacheco D, Klevit RE, and Hahn S (2014). A sequence-specific transcription activator motif and powerful synthetic variants that bind Mediator using a fuzzy protein interface. *Proc. Natl. Acad. Sci. USA* 111, E3506–E3513. [PubMed: 25122681]
- Wimley WC, and White SH (1996). Experimentally determined hydrophobicity scale for proteins at membrane interfaces. *Nat. Struct. Biol.* 3, 842–848. [PubMed: 8836100]
- Wojciak JM, Martinez-Yamout MA, Dyson HJ, and Wright PE (2009). Structural basis for recruitment of CBP/p300 coactivators by STAT1 and STAT2 transactivation domains. *EMBO J.* 28, 948–958. [PubMed: 19214187]

Highlights

- A high-throughput assay quantifies the activities of activation domains in human cells
- Strong acidic activation domains require both acidic and hydrophobic residues
- The combination of acidic and hydrophobic residues predicts new activation domains

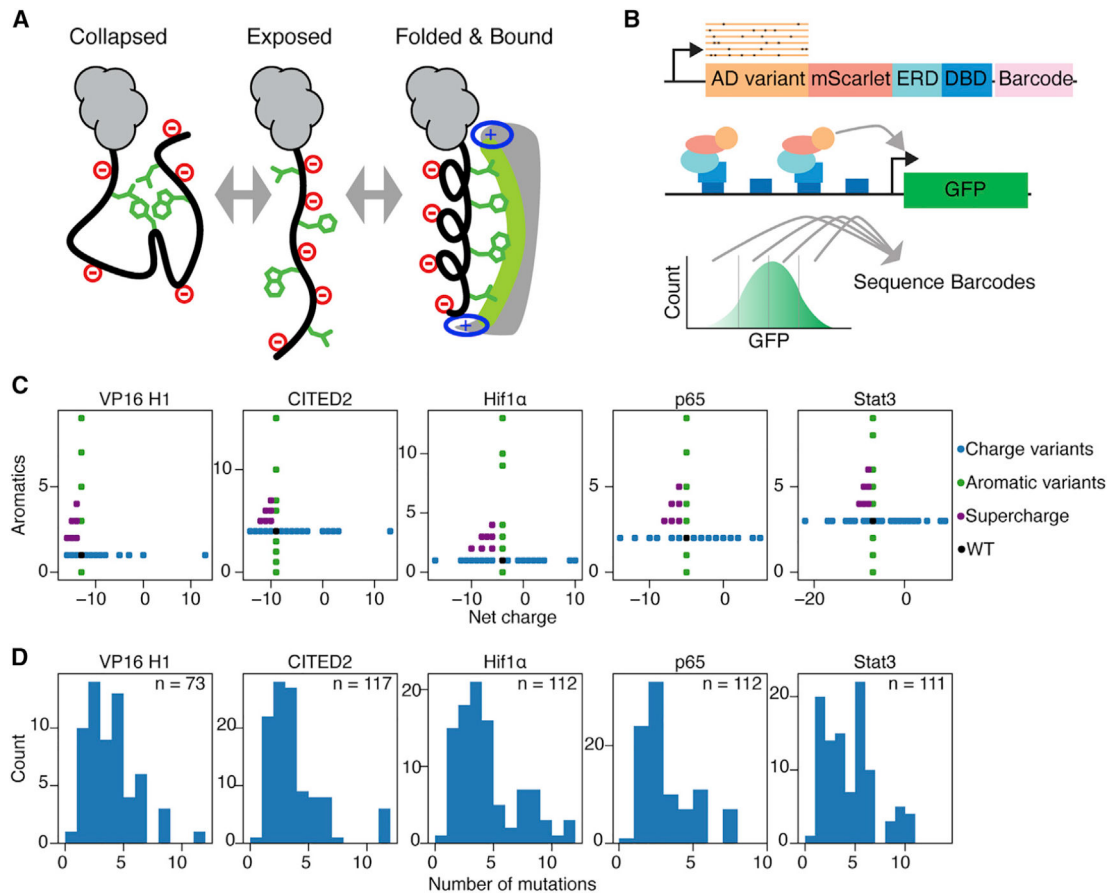


Figure 1. A high-throughput assay for measuring the activities of AD variants in parallel
 (A) In the acidic exposure model, ADs fluctuate between collapsed and exposed states. Exposed ADs can bind coactivators and partially fold.
 (B) The high-throughput AD assay uses a synthetic DNA binding domain (DBD), an estrogen response domain (ERD), a GFP reporter, FACS, and barcode sequencing. The reporter is integrated at the AAVS1 locus.
 (C) We designed mutations that varied the net charge or the number of aromatic residues. We designed a small set of supercharge variants to vary both properties.
 (D) Histograms of the number of mutations in each variant. Most variants had 5 or fewer substitutions.

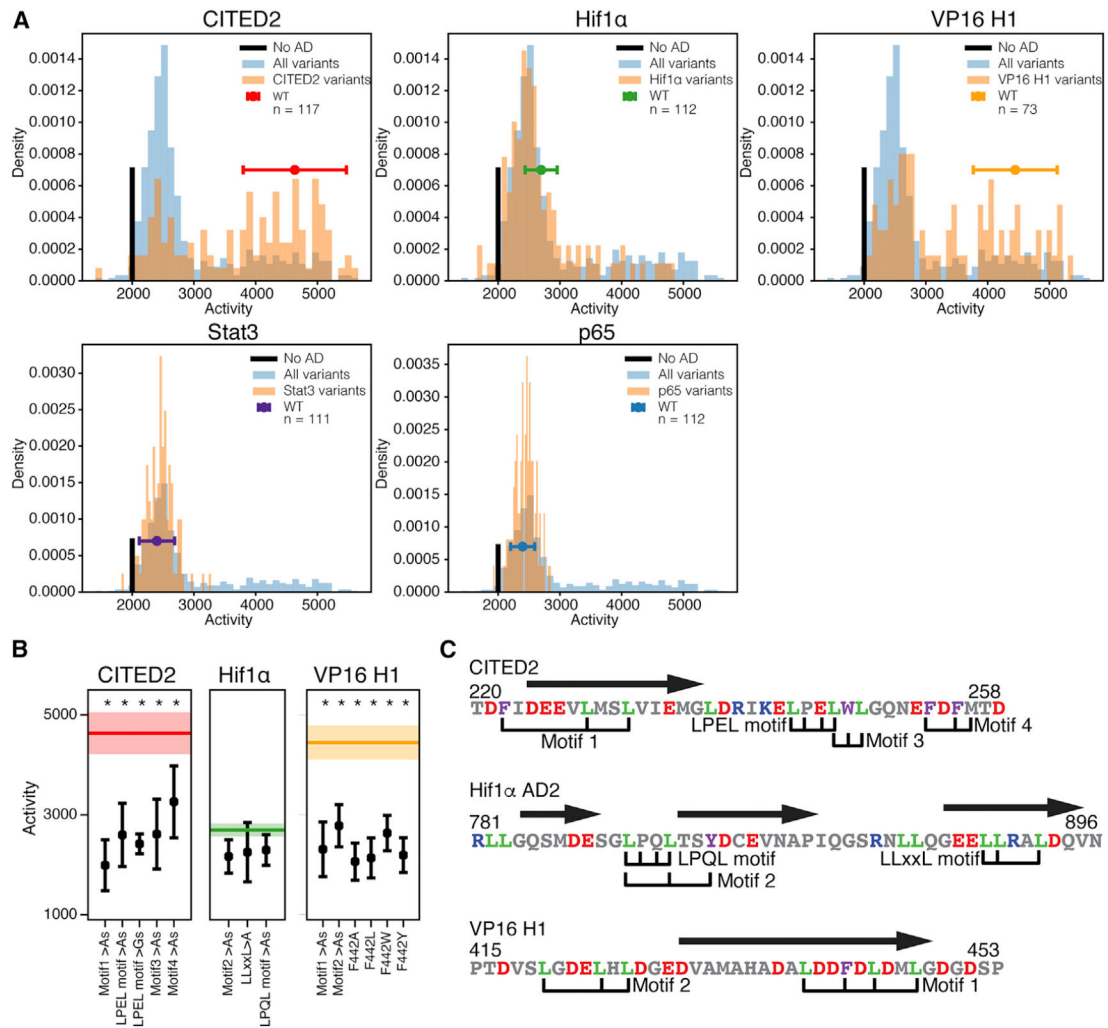


Figure 2. Rationally designed variants increase and decrease AD activity

(A) Histograms of the activities of all variants ($n = 525$, blue) and variants of each AD (orange) are shown. On the x axis, activity is the calculated GFP fluorescence (arbitrary units, AU). On the y axis, density is the normalized counts of variants in each bin of activity. Biological replicates were normalized so that the No AD control had an activity of 2,000 and then averaged together. The vertical black line indicates the activity of the No AD control. For each WT AD, the mean and standard deviation across the four replicates are shown.

(B) The effects of mutating hydrophobic motifs to alanine or glycine residues are shown. For VP16, the effects of substituting aromatic residues with alanine or leucine. For each panel, the thick line is the mean activity of the WT AD and the shaded box is the standard deviation. Colors match (A). *, $p < 0.05$, two-sided t test with 5% FDR correction.

(C) Motif locations and alpha helices (arrows).

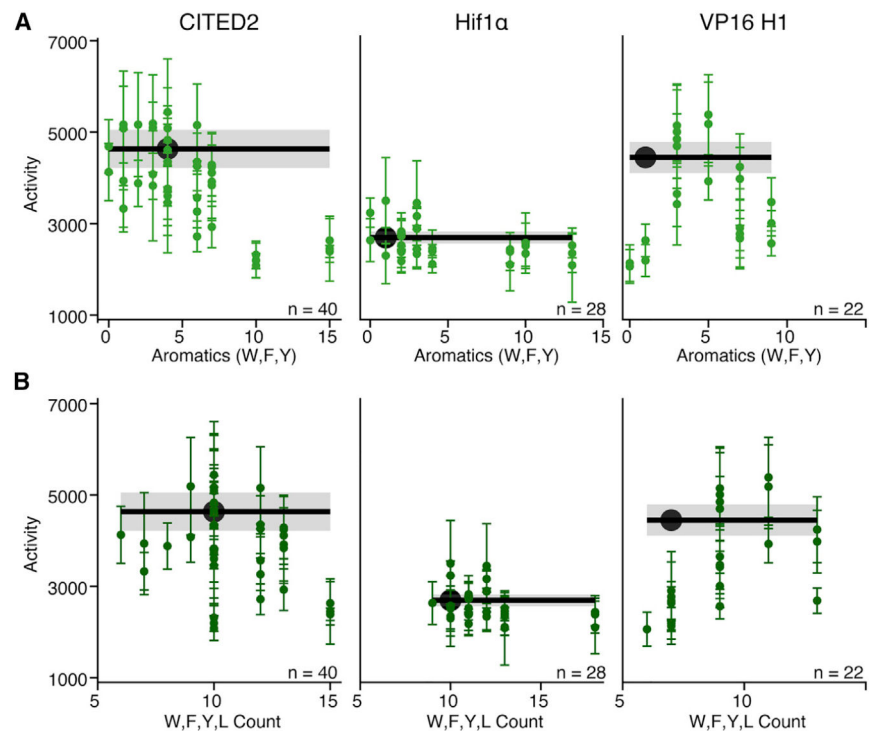


Figure 4. Adding aromatics has context-dependent effects on AD activity

(A) For variants that add or remove aromatic residues, the mean and standard deviation are plotted. Activity (AU) is plotted against the number of aromatic (W,F,Y) residues. WT activity, black dot and line; WT standard deviation, gray box. The relationship between AD activity and the total number of aromatics is complex.

(B) Variants that add or remove aromatic residues are shown with activity plotted against the number of W,F,Y,L residues. Individual points for all variants are shown in Figure S4.

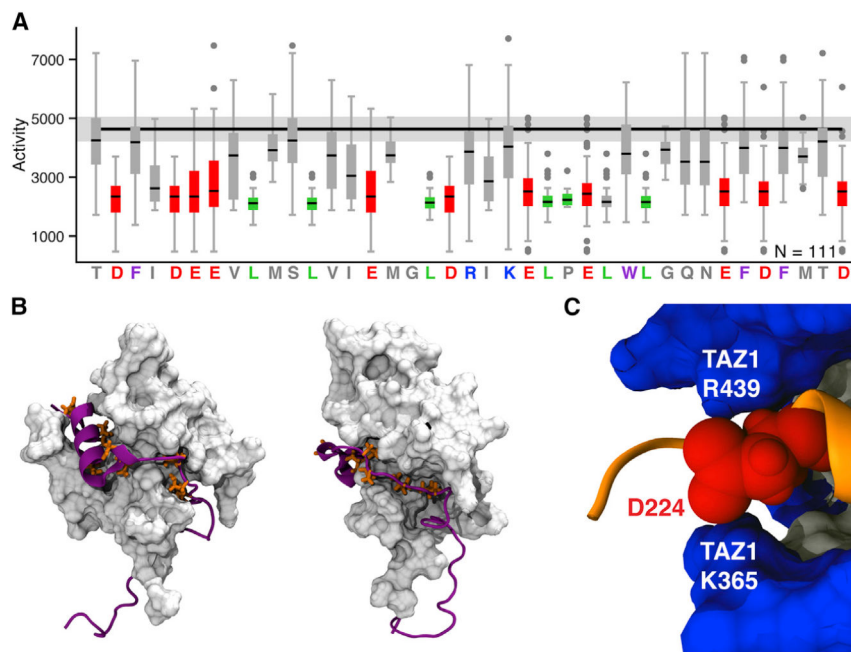


Figure 5. Rational mutagenesis reveals the structural constraints of an AD-coactivator interaction interface

(A) For each position in CITED2, all variants that changed the residue are summarized as a boxplot (activity, AU). Note that each position has different substitutions, and variants with multiple substitutions are included in multiple columns. Acidic (red) and leucine (green) residues make large contributions to AD activity. Medians, black lines. Whiskers are 1.5 times the interquartile range. Outliers, gray dots. WT mean and standard, black line and gray box. This analysis excludes the shuffle variants.

(B) For all the positions in (A) with a median less than 3,000 AU, we visualized these residues (orange) on the NMR structure of CITED2 bound to the TAZ1 coactivator (1R8U). CITED2 backbone, purple; visualized residues, orange; and TAZ1, white. Residues that make large contributions to activity point toward the coactivator surface.

(C) D224 (red) of CITED2 is sandwiched between the narrowest point of the basic rim (blue) of the binding canyon of TAZ1. See Figure S10 for snapshots of all the 20 structures in 1R8U.

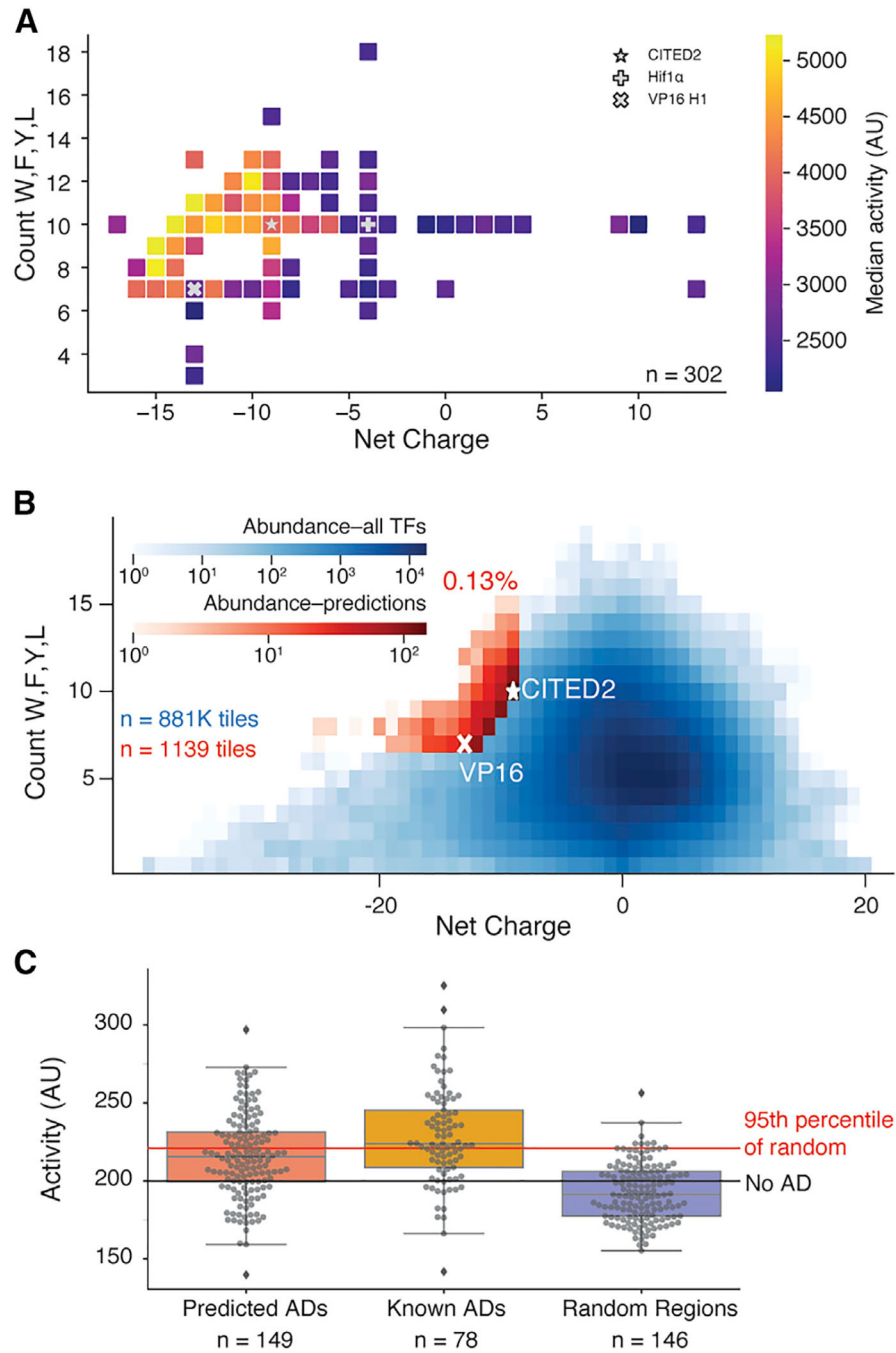


Figure 6. Strong ADs are acidic and contain many W,F,Y,L residues

(A) For each point, the x position indicates the net charge and y position indicates the number of W,F,Y,L residues. Color (AU) indicates the median activity of all variants with each combination (see Figure S11 for all individual variants). All variants of VP16, CITED2, and Hif1α are included (n = 302). The No AD control is 2,000 AU.

(B) A heatmap of all 39 AA tiles from human TFs (log scale). The pixel location indicates the net charge and W,F,Y,L counts, and the blue intensity indicates the number of tiles

with that combination. Only 0.13% of tiles (red, rescaled heatmap) are as extreme or more extreme than VP16 (x) and CITED2 (*). The red tiles peak at CITED2.

(C) TF regions spanned by the red tiles (red, n = 149) are more likely to have AD activity than random regions (blue, n = 146). Most, but not all, published ADs (orange, n = 78) have high activity in this assay. In this experiment the No AD control was normalized to 200 AU. The activities (AU) in panel A are not directly comparable to the activities in panel C. The boxplot shows the quartiles and whiskers are drawn at 1.5 times the interquartile range.

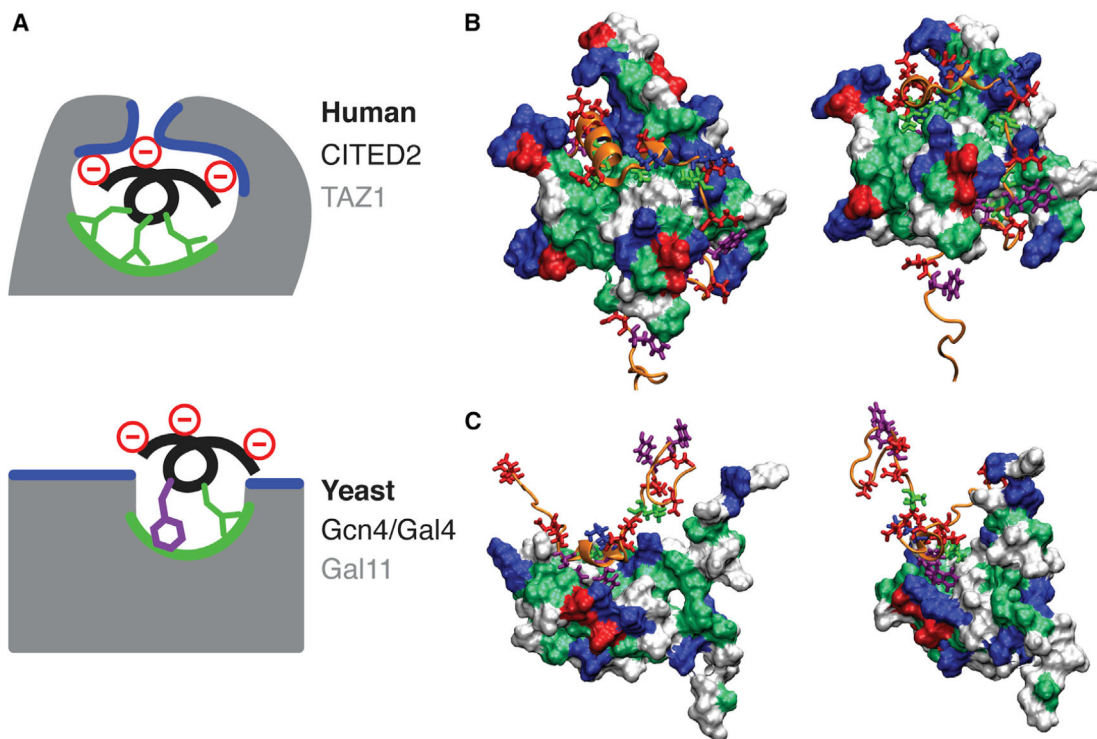


Figure 7. The structure of the coactivator AD-binding canyon constrains AD sequence
 (A) The CITED2 AD is inside the TAZ1 canyon, a structural constraint that favors leucine residues. The yeast Gcn4 AD is outside the Med15/Gal11 canyon, enabling a fuzzy interaction that favors aromatic residues.
 (B) The deep canyon of TAZ1 embraces CITED2 (orange, 1R8U).
 (C) The binding canyon of Gal11 (Med15) is shallow, and the Gcn4 central acidic AD inserts aromatic side chains (2LPB). Colors in (B) and (C) are red, acidic (negative); blue, basic (positive); green, hydrophobic; purple, aromatic; and other, white.

KEY RESOURCES TABLE

REAGENT or RESOURCE	SOURCE	IDENTIFIER
Bacterial and virus strains		
DH5alpha	NEB	C2989
Chemicals, peptides, and recombinant proteins		
β -estradiol	Sigma	E2758
G418 (Neomycin)	Invitrogen	11811031
Puromycin	Sigma	P8833
Critical commercial assays		
ZymoPURE II Plasmid Maxiprep	Zymo	D4202
MACS Dead cell removal kit	Miltenyi Biotec	130-090-101
Deposited data		
Short read sequencing data for Sort-seq approach	This study	NIH GEO: GSE190288
PDB structures	Protein Data Bank	IR8U, 2LPB, 1L8C
Experimental models: Cell lines		
K562 with landing pad	Maricque et al., 2018	LP3
K562 with landing pad and reporter	This study	T7.1E3
Oligonucleotides		
Custom 217bp library for p53 mutagenesis	Agilent	N/A
Custom 217bp library for 5 acidic AD mutagenesis	Agilent	N/A
Custom oPool library for predicted Ads	IDT	N/A
Recombinant DNA		
pMVS223	This study	AddGene: 176293
pMVS184	This study	AddGene: 176294
5 acidic activation domain variant plasmid library	This study	N/A
p53 activation domain variant plasmid library	This study	N/A
Predicted activation domain plasmid library	This study	N/A
Software and algorithms		
LocalCIDER	Holehouse et al., 2017	PMID: 28076807
FLASH	(Mago and Salzberg, 2011)	PMID: 21903629
ols from statsmodels.formula.api	www.statsmodels.org	www.statsmodels.org
SVR from sklearn	Pedregosa et al., 2011	http://scikit-learn.org/
Custom analysis scripts	This study	doi:10.5281/zenodo.5799747
Activation domain predictor	This study	doi:10.5281/zenodo.5794650

REAGENT or RESOURCE	SOURCE	IDENTIFIER
CAMPARI	campari.sourceforge.net	N/A
ABSINTH	Vitalis and Pappu, 2009	PMID: 18506808
VMD	Humphrey et al., 1996	www.ks.uiuc.edu/Research/vmd/
SOURSOP	soursop.readthedocs.io	N/A

Author Manuscript

Author Manuscript

Author Manuscript

Author Manuscript